communications materials

Article

https://doi.org/10.1038/s43246-024-00631-z

Toward direct band gaps in typical 2D transition-metal dichalcogenides junctions via real and energy spaces tuning

Mei-Yan Tian[1], Yu-Meng Gao[1], Yue-Jiao Zhang[1], Meng-Xue Ren[1], Xiao-Huan Lv[1], Ke-Xin Hou[1], Chen-Dong Jin[1,2,3], Hu Zhang[1,2,3], Ru-Qian Lian[1,2,3], Peng-Lai Gong[1,2,3], Rui-Ning Wang[1,2,3], Jiang-Long Wang[1,2,3] ✉ & Xing-Qiang Shi[1,2,3] ✉

Most of the van der Waals homo- and hetero-junctions of group VIB two-dimensional (2D) transition-metal dichalcogenides (TMDs; MoS_2, WS_2, $MoSe_2$, and WSe_2) show indirect energy band gaps which hinders some of their applications especially in optoelectronics. In the current work, we demonstrate that most of the bilayers and even few-layers consisting of group VIB TMDs can have direct gaps by efficient weakening of their interlayer interactions via real and/or energy spaces tuning, which is based on insights from quantitative analyses of interlayer electronic hybridizations. Real space tuning here means introducing large-angle rotational misalignment between layers, which has been realized in a very recent experiment; and, energy space tuning means introducing energy mismatch between layers which can be introduced efficiently by different means thanks to the small vertical dielectric constant of 2D semiconducting TMDs. The efficient tuning in both real and energy spaces proposed here paves an avenue for indirect-direct gap regulation of homo- and hetero-junctions of TMDs and other 2D semiconductors. Notably, both tuning can be permanently preserved and hence our work is of great significance for the diverse applications of 2D semiconductors.

Two-dimensional (2D) layered materials and their homo- and hetero-junctions have ignited great enthusiasm in both fundamental research and potential applications[1–8]. Monolayers of different 2D layered compounds can be stacked on top of each other with no constraints imposed by lattice match or chemistry compatibility[9]. Among them, the 2D transition-metal dichalcogenides (TMDs) homo and hetero-junctions have tunable band structures and promising in electrical and optical applications. TMDs exhibit direct or indirect band gaps and indirect band gap occupies a major portion of the semiconductors[10]. Direct band gap semiconductors have advantageous in photon absorption and emission, ultrafast interlayer photoexcited response[11] and ultrafast (<100 fs) interlayer charge transfer[12] which could be used in the construction of optoelectronic devices, photocatalysis, photoelectric sensor and valleytronic components, etc.[13–18]. Although there have been many studies for band structure modulation of TMDs with different means[6,15,19–37], to achieve direct energy gaps in general bilayer and few-layer TMDs remains challenging.

The monolayers of group VIB TMDs (MoS_2, WS_2, $MoSe_2$, and WSe_2) show direct band gaps at the K point of Brillouin zone (BZ)[38–41] while most of their homo and heterostructures change to indirect gaps[4,42] except for the $MoSe_2/WSe_2$ bilayer[9,11]. The direct–indirect gap transition is correlated to the interlayer electronic hybridizations between orbitals in different layers, dubbed as the quasi-bonding (QB) interaction[43], which is mainly at Γ point for valence band (VB@Γ), and, at Λ point in the middle of Γ–K path for conduction band (CB@Λ) for TMDs[4]. The interlayer QB interaction is a subject of significant interest in many studies[8,43–46] since QB plays a crucial role in shaping 2D materials' electronic and optical properties[42,47]. Very recently, efficiently engineering interlayer interaction in energy space has been proposed[48] in addition to tuning it in real space (e.g., via decrease interlayer separation by pressure)[49].

[1]College of Physics Science and Technology, Hebei University, Baoding, PR China. [2]Key Laboratory of Optic-Electronic Information and Materials of Hebei Province, Baoding, PR China. [3]Hebei Research Center of the Basic Discipline for Computational Physics, Baoding, PR China. ✉e-mail: jlwang@hbu.edu.cn; shixq20hbu@hbu.edu.cn

In the current work, we demonstrate that the TMDs homo and heterobilayers and even few-layers can be tuned to direct gaps by real and/or energy spaces tuning of interlayer interactions, which is based on a classification of the homo and heterobilayers of group VIB TMDs and a basic analysis of the factors that affect band-edge locations in BZ. The real space tuning is achieved by introducing large-angle rotational misalignment between layers, which increases the interlayer separation by ~0.3 Å, decreases the interlayer hopping integral greatly, and make part of the indirect gap bilayers transition to direct gap. All the other bilayers can be further tuned to direct gaps by energy-space tuning, which is applied on top of the real-space tuning by introducing a vertical potential gradient between layers such as by applying external electric field or by dipole-layer adsorption. The energy-space tuning can be introduced efficiently due to the small vertical dielectric constant of 2D semiconducting TMDs[50,51]. Moreover, for few-layer TMDs, direct gaps may also be achieved with our above method. It is important to note that: (1) in contrast to pressure tuning which strengthens interlayer interaction, here our real-space tuning can weaken interlayer interaction; (2) here the large-angle twisting between layers (e.g., 30° ± 8.2°)[52,53] do not induce flat bands, and, it is realized in experiment very recently and reported that large-angle twisted bilayers offer distinctly different platforms from moiré systems[53]; and (3) the direct gap here needs only the band edges tuning back to the K/K′ valley of the component layers, since robust ultrafast interlayer charge transfer has been generally observed in TMDs homo and heterostructures with random rotation angles[11,12,53,54]. The current work not only provides a quantitative understanding of band-edges modulation by tuning interlayer interaction in both real and energy spaces but also offers valuable insights for indirect-to-direct gap tuning of 2D semiconductor homo- and hetero-junctions. More importantly, both real and energy spaces tuning (large-angle twisting and dipole-layer adsorption) can be permanently preserved without the need for external factors to maintain, and hence is of great significance for their multiple applications.

Results and discussion

Classification and basic analyses

The ten bilayers composed of MX_2 (M = Mo, W; X = S, Se) can be classified into "3 + 1" types as indicated in Fig. 1a, b, including three intrinsic types [types (i) to (ii) to (iii)] and one derived type [type-(iv)]. Type-(i) bilayers are homo ones, and, types (ii)/(iii) are hetero ones with lattice match/mismatch, respectively. For type-(i) [Fig. 1a(i)], there are four homobilayers composed of MX_2/MX_2 (M = Mo, W; X = S, Se) as indicated by blue lines in Fig. 1b. For type-(ii) [Fig. 1a(ii)], there are two heterobilayers composed of MoX_2/WX_2 (with different M elements and a same X element) as indicated by black lines in Fig. 1b. Type-(ii) heterobilayers exhibit minimal lattice mismatch (~0.04%) and hence form lattice-matched bilayers. For type-(iii) [Fig. 1a(iii)], there are four heterobilayers of MS_2/MSe_2 (with Se and S elements, respectively, in the two component layers of bilayer, while the M elements in component layers can be either same or different) as indicated by red lines in Fig. 1b. These four heterobilayers all have ~4% lattice mismatch between component layers. The component layer with Se has larger lattice constants than the component layer with S. This is because, for our studies MX_2s, when the X elements changing from S to Se, the lattice

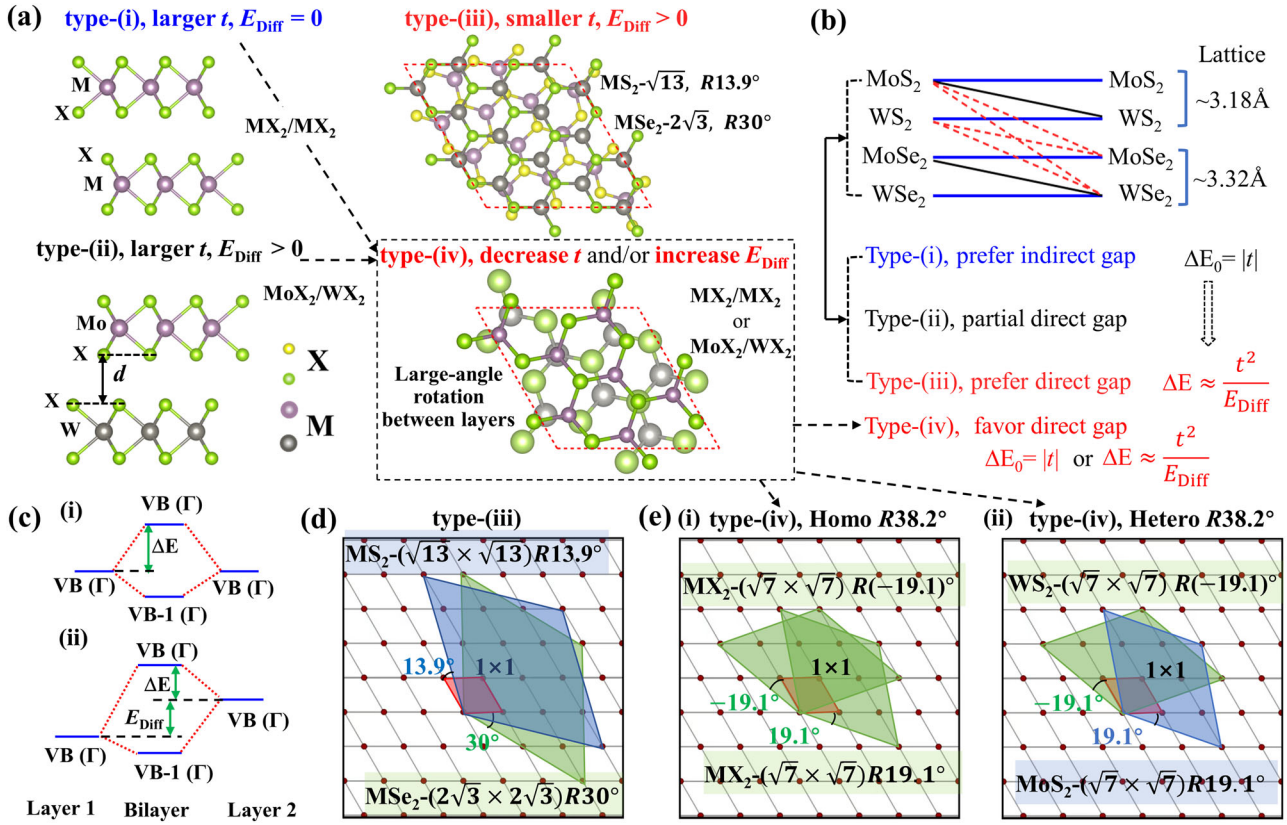

Fig. 1 | The "3 + 1" types of MX_2 bilayers (M = Mo, W; X = S, Se): classification, interlayer-interaction-induced band edge change, and (super)cells. a, **b** Three intrinsic types, (i) to (ii) to (iii), and one derived type-(iv) from types (i) and (ii) with tuning in real and/or energy spaces: type-(i), homobilayers with larger interlayer hopping integral ($|t|$) and zero energy difference ($E_{Diff} = 0$) between layers, which prefer indirect gaps; type-(ii), heterobilayers with the same X atoms between layers which have larger $|t|$ while $E_{Diff} \neq 0$; type-(iii), heterobilayers with different X atoms with supercells (see text), which have smaller $|t|$ and $E_{Diff} \neq 0$, and prefer direct gaps; type-(iv) is the derived type from types (i) and (ii) by decreasing $|t|$ and/or increasing E_{Diff} between layers (see text). **c** Sketches for the interlayer-interaction-induced band edge change from monolayer to bilayer [ΔE in (**b**)] using VB@Γ (ΔE_Γ) as the example for homobilayers (i) and heterobilayers (ii). **d**, **e** Supercells used for type-(iii) heterobilayers and for type-(iv) homo(hetero)-bilayers with 38.2° twist angle between layers as an example. In (**d**, **e**) supercells of the two layers are shown with a relative rotation, while in (**a**)(iii) and (**a**)(iv) the supercells are aligned and the atomic structure between layers is rotated relatively.

Table 1 | Energy difference between layers (E_{Diff}) in types (ii) and (iii) and the hopping integral between layers ($|t|$) in types (i) and (iv)

E_{Diff} (eV)	Type-(ii)	MoS_2/WS_2		$MoSe_2/WSe_2$	
		0.19		0.21	
	Type-(iii)	$MoS_2/MoSe_2$	WS_2/WSe_2	MoS_2/WSe_2	$MoSe_2/WS_2$
		0.37	0.38	0.57	0.17
Energy of X/M atoms (eV)		S 3*p*	Se 4*p*	Mo 4*d*	W 5*d*
		−7.01	−6.51	−3.75	−3.32

$\|t\|$ (eV)	Unitcell	Supercell[a]	Weaken ratio
MoS_2 bilayer	0.50	0.39	78%
WS_2 bilayer	0.42	0.33	78%
$MoSe_2$ bilayer	0.51	0.40	77%
WSe_2 bilayer	0.47	0.34	74%

E_{Diff} values between band edges of VB@Γ in the component layers of types (ii) and (iii) bilayers; and $|t|$ values of VB@Γ in MX_2 bilayers. For E_{Diff}, the corresponding *p*- and *d*-orbital energy levels from pseudopotentials for *X* and *M* atoms of MX_2 are also given as a reference. For $|t|$, the weaken ration is the $|t|$ from supercell (with larger-angle twisting between layers) divided by that from the corresponding $|t|$ of unitcell.

[a]The $|t|$ of supercell is obtained from MX_2 bilayer in the $(\sqrt{7}\times\sqrt{7})R38.2°$structure [refer to Fig. 1a(iv)].

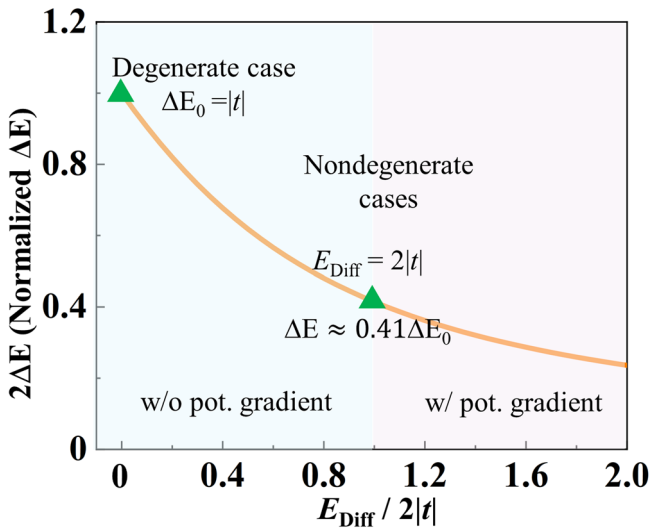

Fig. 2 | The VB@Γ up-shift in energy (Δ*E*) from monolayer to bilayer decreases monotonously with the increase of E_{Diff} relative to $|t|$. In types (ii) and (iii) bilayers $E_{Diff}/|2t| < 1$, and, $E_{Diff}/|2t|$ can be larger than one with applied potential gradient between layers in type-(iv) bilayers. For CB@Λ, similar conclusion holds.

constant is enlarged by about ~4%; while the *M* elements (from Mo to W) almost does not affect lattice constant[55].

The lattice mismatch can be largely removed by constructing supercells of MS_2-$\left(\sqrt{13}\times\sqrt{13}\right)R13.9°$/$MSe_2$-$\left(2\sqrt{3}\times2\sqrt{3}\right)R30°$[55,56], as shown in Fig. 1a(iii), d; with supercells the largest lattice mismatch is then <0.2%. The type-(iv) bilayers [Fig. 1a(iv), b] is a derived type from types (i) and (ii) with real and/or energy spaces tuning (will be discussed later).

For type-(i) [Fig. 1a(i), b], they are homobilayers and hence the component layers match in both real space (lattice and atomic structure) and energy space [$E_{Diff} = 0$ for band edges between layers, refer to Fig. 1c]. The real-space matching results in a relatively smaller interlayer separation and hence larger interlayer hopping integral (i.e., larger $|t|$)[48]. Type-(ii) bilayers are heterobilayers with different *M* elements and a same *X* element, the component layers are different in band-edge energies ($E_{Diff} \neq 0$, namely, energy-space mismatch) but with essentially the same lattice constant (namely, real-space match) and hence still have larger $|t|$. For type-(iii) bilayers with different *X* atoms, the component layers are mismatched in both band-edge energy ($E_{Diff} \neq 0$) and real-space lattice. As a result of real-space mismatch, the average interlayer separation is increased by ~0.3 Å relative to that in types (i) and (ii) [see Supplementary Table 1] and hence results in the decrease of interlayer hopping integral (smaller $|t|$). For bilayers with supercells, the average interlayer separation is the height difference between the average heights of *X* atoms in adjacent layers across the van der Waals (vdW) gap. For the lattice matched ones in Fig. 1a(i)–(ii), unitcells are used; while for the ones with lattice mismatch in Fig. 1a(iii)–(iv), supercells are used. Note that in Fig. 1a(iv), the real-space matched types (i) and (ii) bilayers change to mismatched in real space due to rotational misalignment (larger-angle twisting) between layers; also, the energy matching (E_{Diff}) can also be tuned by introducing vertical potential gradient between layers (details see below).

The different types of bilayers are summarized in Fig. 1b. In type-(i) bilayers, the energy levels from the component layers are degenerate, and, the interlayer-QB-induced up-shift (Δ*E*) of valence band edge at Γ point[4] is equal to the interlayer hopping integral, namely, $\Delta E_0 = |t|$, where the subscript "0" means $E_{Diff} = 0$ [see Supplementary Note 1]. The Δ*E* from monolayer to bilayer using VB@Γ (ΔE_Γ) as the example for homo and heterobilayers are indicated in Fig. 1c(i) and (ii), respectively. For types (ii) and (iii) bilayers in Fig. 1a, b, they have energy differences ($E_{Diff} \neq 0$) between layers as indicated in Fig. 1c(ii). The E_{Diff} and $|t|$ values of some bilayers are listed in Table 1. If $|t| << E_{Diff}$, the band edge up-shift (Δ*E*) can be approximated as $\Delta E \approx \frac{t^2}{E_{Diff}}$. For general cases, including $|t|$ larger than or comparable to E_{Diff}, Fig. 2 shows that Δ*E* decreases monotonously with the increase of E_{Diff} relative to $|t|$; also refer to Supplementary Note 1. We use the two formulae in Fig. 1b to simplify thinking, from which qualitatively correct understanding can be given. More discussion can be found in Supplementary Note 1.

The interlayer separation increases (*d*) increases in types (iii) bilayers by ~0.3 Å, and hence $|t|$ decreases as indicated in Table 1. For type-(ii) bilayers, they are energy mismatched while lattice matched, and hence they are at the intermediate of types (i) and (iii). Based on the above analysis, type-(i) bilayers tend to form indirect band gaps since the stronger interlayer QB interaction may change the band edges from K point to Γ point[4], while type-(iii) bilayers may favor direct band gaps due to the weakened interlayer interaction in both real and energy spaces.

To obtain direct band gaps for types (i) and (ii) structures, we also weaken their interlayer interactions by tuning the interlayer electronic coupling in real and/or energy spaces; and this is the derived type-(iv) in Fig. 1a, b. Here, the real-space tuning means increasing the interlayer separation by a large rotation angle between layers (e.g., $\theta_t = 30° \pm 8.2°$)[30–32,53], the interlayer separation is then increased (Supplementary Table 2) and the interlayer hopping integral $|t|$ is weakened (refer to Table 1). The possible experimental growth method of larger θ_t bilayers[31,53] that we studied is also discussed briefly in Supplementary Note 2. Here, the hopping integral of interlayer sulfur *p*-orbitals (mainly *ppσ*) is inversely proportional to the square of the interlayer separation ($t_{pp\sigma} \propto \frac{1}{d^2}$)[57]. In our calculations, an increase of ~10% in interlayer separation (Supplementary Table 2) reduces interlayer interaction to ~75% (Table 1), which is conducive to the formation of a direct band gap. Supplementary Table 3 provides the summary of bilayers for lattice size, lattice mismatch, energy difference between layers (E_{Diff}), interlayer hopping integral ($|t|$), interlayer vertical separation (d_{M-M} and d_{X-X}), interlayer binding energy (E_B), and twist angle between layers (θ_t). The energy-space tuning means increase E_{Diff}, which can be achieved by introducing a vertical potential gradient between layers and hence introduce (increase) E_{Diff} between homo (hetero) layers and thus also decrease the interlayer interaction. It has been demonstrated that a vertical potential gradient can be applied between layers by such as an external electric field[34–37] or a polar/ferroelectric layer vdW adsorption[48,58], which may significantly increase E_{Diff} due to the small vertical dielectric constant of 2D semiconducting TMDs[50,51].

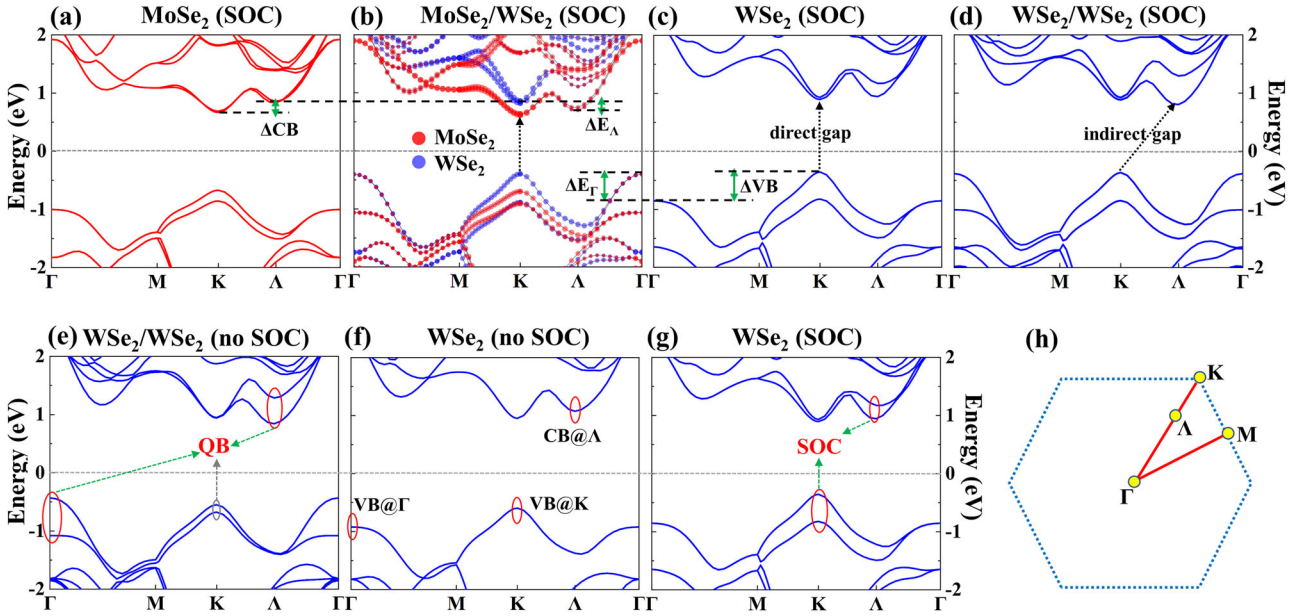

Fig. 3 | Band edge changes in types (i) and (ii) bilayers, and intra- and interlayer factors that affect the band edges. Band edge changes from monolayer(s) to bilayer in (**a**–**c**) for type-(ii) bilayer and in (**c**, **d**) for type-(i) bilayer using $MoSe_2/WSe_2$ heterobilayer and WSe_2 homobilayer as examples. The factors that affect band edges are labeled out in (**a**–**c**) and (**e**–**g**), see text for details. (**c**) and (**g**) are repeated for the convenience of comparing between figures on the same line. **h** Brillouin zone (BZ) with the relevant k points indicated. To compare the energy changes from monolayers to bilayer, the band energies are corrected by the vacuum level changes from monolayer to bilayer and the interface dipole across vdW gap of heterobilayer (see Supplementary Note 3 for detail).

Verification from detailed band structure analysis

To verify the above basic analysis and to give a deeper understanding on the intra- and interlayer factors that govern the band edges, density-functional theory (DFT) band structure calculations including spin–orbit coupling (SOC) are performed. Beginning from types (i) and (ii) bilayers to provide general insights, then to type-(iii) with band unfolding, and finally about the derived type-(iv) bilayers with tuning in real and energy spaces.

Figure 3 (and Supplementary Fig. 1) shows the band structures of bilayers with larger $|t|$, namely, types (ii) and (i) in Fig. 1a, b including two heterobilayers with nonzero $E_{\rm Diff}$ and four homobilayers with zero $E_{\rm Diff}$. As typical examples, Fig. 3b, d shows the band structures of $MoSe_2/WSe_2$ heterobilayer and WSe_2 homobilayer, and, the component monolayers' band structures are shown in Fig. 3a, c as references. Figure 3 and Supplementary Fig. 1 show that, except for $MoSe_2/WSe_2$, all the other five bilayers have an indirect band gap—just as that expected in Fig. 1b for types (i) and (ii) bilayers with larger $|t|$. The $MoSe_2/WSe_2$ bilayer shows direct band gap, which is consistent with the experimental and theoretical literatures[9,11].

The factors that affect band-edge locations [namely, the K, Γ, or Λ point of BZ] are indicated in Fig. 3a–g, which include: (1) ΔE_Γ and ΔE_Λ as indicated in Fig. 3b, which is the band edges change of VB@Γ and CB@Λ from monolayers to bilayer due to the interlayer QB interaction [comparing Fig. 3e, f, which show the effect of interlayer QB on VB@Γ and CB@Λ]; and, (2) ΔCB and ΔVB in Fig. 3a, c which is the energy difference within monolayers' VB and CB edges and is related to SOC [comparing Fig. 3f, g which show the SOC effect on VB@K and CB@Λ]. The ΔVB in Fig. 3c is the energy difference between VB@K and VB@Γ, and the ΔCB in Fig. 3a is the energy difference between CB@K and CB@Λ. Larger SOC increases the size of ΔVB but decreases that of ΔCB (or even change the sign of ΔCB in bilayer, as a combination of effects from both SOC and interlayer QB). The interlayer QB effect on VB@K is less apparent than on VB@Γ and CB@Λ [Fig. 3e], and the reason is given below.

In the following, we discuss the factors that affect band-edge locations in BZ from the above-mentioned two main aspects: the SOC effect within monolayer and the interlayer QB interaction.

(i) The SOC effect within monolayer: band structures of component monolayers of bilayer are used as references to see the band structure evolution in different bilayers. For monolayer H-phase TMDs, the VB@Γ is a antibonding state of p_z–d_{z^2} orbitals[43], VB@K is composed of $p_{x,y}$ and d_{xy,x^2-y^2} orbitals, CB@K mainly has $p_{x,y}$ and d_{z^2} orbitals, and CB@Λ is composed of all p, d_{xy,x^2-y^2} and d_{z^2} orbitals[4]. For the SOC effect, both the atomic number (Z) and the magnetic quantum number (m_l) are relevant. Among the four MX_2 studied here, WSe_2 with heavier elements has the most significant SOC effect; and, the atomic number of W ($Z = 74$) is much larger than that of Se ($Z = 34$) and hence the SOC effect mainly from the W d-orbitals. Also, note that $m_l = 0$ for d_{z^2} orbital and $|m_l| = 2$ for d_{xy,x^2-y^2} orbitals. From the above-mentioned band edge orbital-characters (d_{z^2} orbital at VB@Γ and CB@K, and d_{xy,x^2-y^2} for VB@K and CB@Λ), the SOC effect is evident mainly at the band edges of VB@K and CB@Λ, which is confirmed by comparing Fig. 3f, g. The SOC effect causes the band splitting of VB@K and CB@Λ within monolayer especially for VB@K, which shifts-up VB@K and favors the valence band maximum (VBM) at the K point. For WSe_2, the SOC splitting is about 0.47 eV and it shifts-up VB@K energy by 0.24 eV. Namely, the SOC effect favors the formation of direct band gap at K point. However, the shifts down of CB@Λ within monolayer due to SOC favors the conduction band maximum (CBM) at the Λ point in WSe_2, especially for bilayer [Fig. 3c, d].

(ii) The interlayer QB interaction: from monolayer to bilayer, the changes in band edges are due to the interlayer QB interaction at and around VB@Γ and CB@Λ [comparing Fig. 3e and f] due to the interlayer interactions of out-of-plane p_z orbitals of X atoms across the vdW gap since they are close in real space (details see below). Under interlayer QB interaction, the VBM tends to changes from K point to Γ point and the CBM tends to shifts from K to Λ point. The interlayer orbital couplings is weak for the band edges at K point from symmetry analyses[59], and hence the energy changes at K point are minimal for VB@K and CB@K. For the simplicity of discussion, for interlayer QB we focus on the VB@Γ and CB@Λ, and the ΔEs in Figs. 1c and 3b denote the more apparent band-edge energy changes of VB@Γ and CB@Λ from monolayer to bilayer.

To quantify the band-edge changes from monolayer to bilayer for types (i) and (ii) bilayers, the sizes of ΔE_Γ vs ΔVB and ΔE_Λ vs ΔCB are given in Table 2, which show that: ΔE_Γ (ΔVB) are in the range of 0.39–0.51 eV (0.06–0.50 eV), and, ΔE_Λ (ΔCB) are in the range of 0.07–0.22 eV

(0.06–0.24 eV). The monolayers with larger ΔVB values (~0.5 eV) help to maintain the VB edge at K point from monolayer to bilayer. However, if $\Delta E_\Gamma > \Delta VB$, the VB edge shifts from K point to Γ point, as shown in the last column of Table 2. Similarly, the CB band edge shifts from K to Λ point if $\Delta E_\Lambda > \Delta CB$.

For type-(ii) bilayer, using $MoSe_2/WSe_2$ as the example, the interlayer separation of the heterobilayer almost equal to that of the two corresponding homobilayers of $MoSe_2$ and WSe_2 (refer to Supplementary Table 1). However, in Table 2, the ΔE_Γ value for $MoSe_2/WSe_2$ heterobilayer (of 0.45 eV) is smaller than the average of ΔE_Γ of $MoSe_2$ and WSe_2 homobilayers ($\frac{0.51+0.47}{2} = 0.49$ eV). This is due to the interlayer energy difference ($E_{Diff} \neq 0$) in heterobilayer, which weaken the interlayer QB as indicated in Fig. 2. For the other heterobilayer in Table 2, MoS_2/WS_2, the same conclusion holds. This conclusion also applies for ΔE_Λ of the conductance band (Table 2). These indicate that the QB interaction in type-(ii) bilayers is weaker compared to type-(i), and favor the formation of a direct band gap in heterobilayer compared to homobilayer.

Table 2 | Energy changes of ΔE_Γ in VB (ΔE_Λ in CB) from monolayer to bilayer vs ΔVB (ΔCB) in monolayer(s) for types (i) and (ii) bilayers, and the resulted band-edge location in BZ

BL-TMDs	ΔE_Γ, ΔVB (eV)	ΔE_Λ, ΔCB (eV)	VB–CB location
$MoSe_2/MoSe_2$	0.51, 0.33	0.22, 0.17	Γ–Λ
WSe_2/WSe_2	0.47, 0.50	0.14, 0.06	K–Λ
$MoSe_2/WSe_2$	0.45, 0.50 (VB@WSe_2)	0.12, 0.17 (CB@$MoSe_2$)	K–K
MoS_2/MoS_2	0.50, 0.06	0.18, 0.24	Γ–K
WS_2/WS_2	0.42, 0.25	0.09, 0.10	Γ–K
MoS_2/WS_2	0.39, 0.25 (VB@WS_2)	0.07, 0.24 (CB@MoS_2)	Γ–K

For type-(ii) heterobilayers, only the monolayer that contributes to the bilayer band edges are needed, as indicated in parentheses. The resulted bilayer band-edge locations for VB and CB are listed in the last column; Γ–Λ means VB@Γ and CB@Λ, and so on; note that for monolayers, the band-edge location is always K–K.

The -*p*COHP analysis (details see Supplementary Table 4) helps to understand the orbital-contribution to interlayer QB interactions, namely, which orbital of which atom dominates the interlayer interaction. The magnitude of -*p*COHP values in Supplementary Table 4, taking $MoSe_2/WSe_2$ as an example, indicate that the interlayer Se-p_z orbitals dominate the interlayer interaction at VB@Γ; while for CB@Λ both out-of-plane and in-plane *p*-orbitals of Se are involved. Since Se orbitals dominate interlayer interaction, namely, the *X* atoms from adjacent layers dominate interlayer orbital-hybridization because they are close in real-space[43,60,61], we give d_{x-x} in Supplementary Tables 1–3.

Now move to type-(iii) bilayers. The layer-projected band structures of the type-(iii) bilayers with MS_2-$(\sqrt{13}\times\sqrt{13})R13.9^\circ$/$MSe_2$-$(2\sqrt{3}\times2\sqrt{3})R30^\circ$ supercells (in short MS_2/MSe_2 supercell) are shown in Fig. 4b, c and Supplementary Fig. 2, which show that the VB (CB) edge is contributed by the MSe_2 (MS_2) layer especially for MoS_2/WSe_2 in Fig. 4b, c, forming type II band alignments. To see clearly the band edge locations in BZ (namely, at K point or not) for the supercell structures, one need to unfold the supercell band structure from supercell BZ to unitcell BZ[62]. For the $\sqrt{13}$ supercell, as indicated in Fig. 4a, the K point of unitcell is folded to K_S point of supercell. However, for the $2\sqrt{3}$ supercell, as indicated in Fig. 4d, the K point of unitcell is folded to Γ_S point of supercell, which makes the VB edge in Fig. 4c folded to the Γ_S point of supercell BZ, which can be unfolded back to the K point of unitcell BZ [see Fig. 4d, g]. The band structures in Fig. 4b, c with supercell BZs are unfolded to Fig. 4f, g with unitcell BZ, respectively, which show that the CB@K (VB@K) of MoS_2 (WSe_2) contributes to the bilayer CB and VB edges, respectively. Namely, the type-(iii) MoS_2/WSe_2 bilayer form direct gaps. The same conclusion (that form direct gaps) holds for all of the four type-(iii) bilayers, just as expected in Fig. 1b, and Supplementary Table 5 provides the detailed data (similar to the analysis method of Table 2). In Fig. 4e, h, the band structures of isolated monolayers are also given as references. Note that Fig. 4a, d gives the BZs of

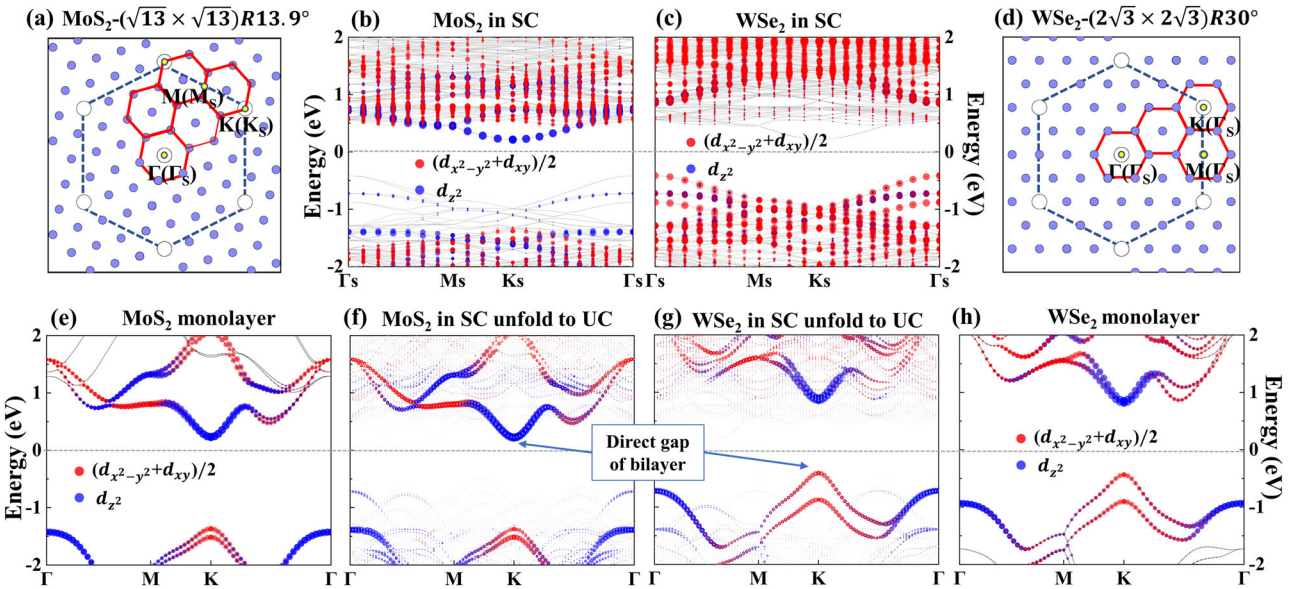

Fig. 4 | Direct band gaps in type-(iii) bilayers and band structure unfolding using the MoS_2-$(\sqrt{13}\times\sqrt{13})R13.9^\circ$/$WSe_2$-$(2\sqrt{3}\times2\sqrt{3})R30^\circ$ supercell (in short, the MoS_2/WSe_2 SC) as the example. BZ folding between unitcell (UC) and $\sqrt{13}$, $2\sqrt{3}$ supercells in (**a**, **d**); and, the layer-projected band structures of the MoS_2 and WSe_2 layer in the MoS_2/WSe_2 SC (**b**, **c**): the VB (CB) edge of bilayer is from WSe_2 (MoS_2), forming type II band alignment. In (**a**, **d**), larger (smaller) hexagon represents the BZ of unitcell (supercell) and the *k*-points of supercell has a subscript "S". For the $2\sqrt{3}$ supercell in (**d**), K point of unitcell is folded to Γ_S point of supercell, which makes the VB edge from WSe_2 folded to the Γ_S point in (**c**) and unfolded back to the K point in (**g**). The band structures in (**b**) and (**c**) are unfolded to (**f**) and (**g**), respectively, which show that the MoS_2/WSe_2 bilayer form direct gap at K point. Comparison of band structures of isolated monolayers with that in SC: **e**, **f** for MoS_2 and **g**, **h** for WSe_2. Band structures projected to $d_{x^2-y^2} + d_{xy}$ and d_{z^2} orbitals are shown with dots and the dot sizes indicate the relative magnitude of projection.

unitcell and $\sqrt{13}$, $2\sqrt{3}$ supercells, another representation[53] is given in Supplementary Fig. 3, which give the same conclusion for BZ folding.

In summary, the above detailed band structure analysis confirmed that, just as expected in Fig. 1b, all type-(i) bilayers exhibit indirect band gaps, partial type-(ii) bilayer shows a direct band gap, and all type-(iii) bilayers have direct band gaps. The interlayer separation in type-(iii) bilayers is increased by ~0.3 Å than that in type-(i) bilayers (Supplementary Table 1), and thus type-(iii) bilayers have smaller interlayer hopping integral $|t|$. In addition, heterobilayers have an energy difference between layers ($E_{\mathrm{Diff}} \neq 0$). Both smaller $|t|$ and E_{Diff} weaken the effect of interlayer QB interaction (refer to Fig. 2) and facilitate the formation of direct band gaps for type-(iii) bilayers.

Real and energy spaces tuning

For type-(iii) bilayers, two factors (smaller $|t|$ and nonzero E_{Diff}) weaken the effect of interlayer interaction on band edge changes in BZ, and all type-(iii) bilayers show direct band gaps. Inspired by this, for all type-(i) and the one type-(ii) bilayer, MoS_2/WS_2, that has indirect gaps, we weaken their interlayer interaction by real and/or energy spaces tuning (namely, decreasing $|t|$ and/or increasing E_{Diff}), and this forms the derived type-(iv) bilayers in Fig. 1a(iv). Here, real-space tuning means introducing large twisting angles (θ_t) between layers which increase the interlayer separation and decreases the hopping integral $|t|$, and, energy-space mismatch (E_{Diff}) between layers can be introduced with different means which also weaken the interlayer interaction. The E_{Diff} can be introduced (enhanced) by a vertical potential gradient between layers, such as by applying an external vertical electric field or via dipole-layer vdW adsorption[34,35,58].

Figure 5 (and Supplementary Fig. 4, Supplementary Table 6) shows that direct band gaps are obtained with only the real-space tuning or with energy-space tuning combined with real-space tuning. The BZ folding is given in Supplementary Fig. 5a, which shows that the K point of unitcell is folded to the K_S point of $\sqrt{7}$ supercell. So, we can judge direct gap or not directly from the band structure of $\sqrt{7}$ supercell. For real-space tuning [refer to Fig. 1e], $\sqrt{7}$ supercells are constructed with interlayer twisting angle $\theta_t = 38.2°$ [53]; and for energy-space tuning a vertical electric field or dipole-layer vdW adsorption (Supplementary Note 5 which includes Supplementary Fig. 6) are used. For most cases, only a small electric field of 0.1–0.2 eV Å^{-1} is needed to obtain direct gaps (Supplementary Table 6). For MoS_2 bilayer, strain is also introduced in addition to the normal real and energy spaces regulation (Supplementary Note 6 and Supplementary Fig. 7) and Supplementary Table 6 provides the detailed data.

Comparing Figs. 5a and 3d, for the WSe_2 homobilayer with and without large-angle rotation between layers, shows that the WSe_2 homobilayer undergoes an indirect-to-direct gap transition. Supplementary Fig. 8 shows that with another interlayer rotation angle, $\theta_t = 21.8°$, the WSe_2 large-angle twisted homobilayer also has a direct gap. Supplementary Table 2 demonstrates that the interlayer separations in type-(iv) bilayers with interlayer rotation have also increased by ~0.3 Å compared to the corresponding unrotated bilayers, which weaken the interlayer interactions by decreasing $|t|$; and hence favor direct gaps, as expected in Fig. 1a(iv), b.

For the other type-(iv) bilayers and trilayers, to obtain direct gaps, energy-space (E_{Diff}) tuning is also needed in addition to the above real-space tuning of interlayer separation [Fig. 5b–d and Supplementary Fig. 4]. The critical electric field (E_{Field}) to obtain direct gap is ~0.2 eV Å^{-1} for bilayer and ~0.3 eV Å^{-1} for trilayer. For trilayer, the interlayer QB induced energy up-shift of VB@Γ increases a bit relative to that in bilayer[4], and hence the critical E_{Field} to obtain a direct gap is a bit larger for trilayer. For even-thicker layers, since the additional up-shift of VB@Γ is not significant[4], one expect that the critical E_{Field} will not change much with layer number (also see the subsection below).

Figure 5c demonstrates that ΔE_{Diff} increases by 0.10–0.14 eV per 0.1 eV Å^{-1} E_{Field}, implying that the electric field can efficiently increase E_{Diff} and weaken the interlayer interaction. In Supplementary Note 5, we present that the potential gradient can also by applied by dipole-layer vdW adsorption and the dipole-layer-induced equivalent E_{Field} is given. Also, direct gap is obtained by dipole-layer vdW adsorption.

From the partial charge density of band edges shown in Fig. 5e, it can be seen that under the influence of vertical electric field, VB@Γ_S is primarily contributed by the top two layers, while CB@K_S is mainly contributed by the bottom layer. Due to the competition between interlayer QB interaction

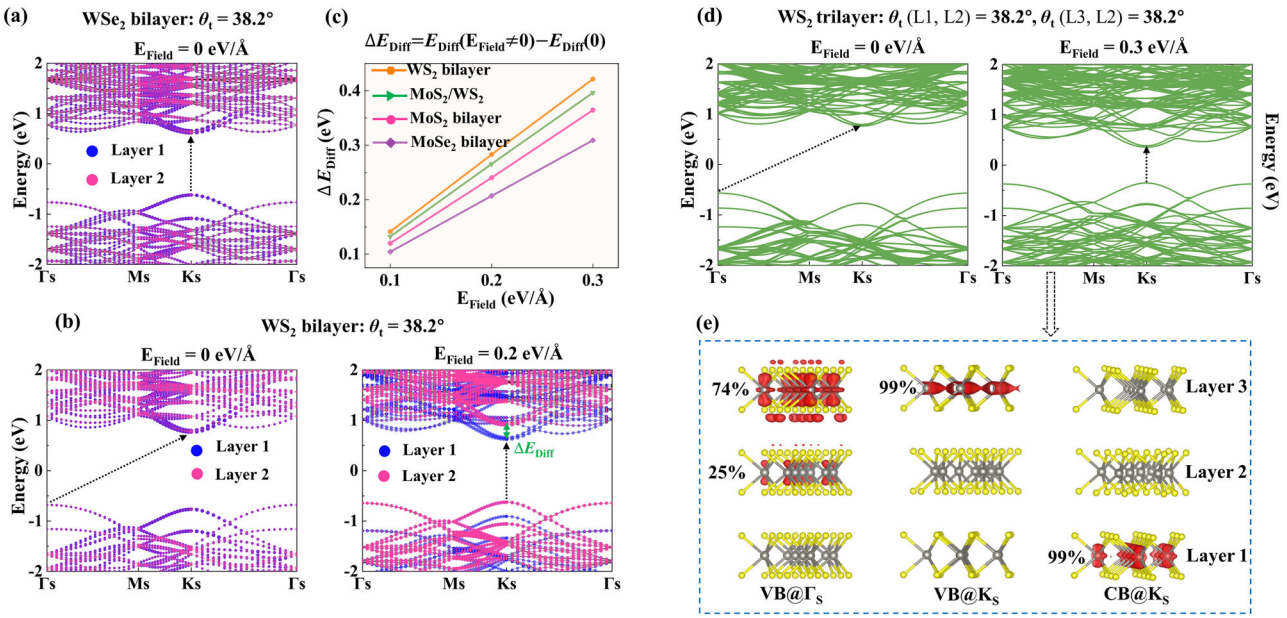

Fig. 5 | The derived type-(iv) bilayers and trilayers with real and energy spaces tuning: direct gaps with small external electric field (E_{Field}). For real-space tuning [refer to Fig. 1e], $\sqrt{7}$ supercells are constructed with interlayer twisting angle of $\theta_t = 38.2°$ as the example; for energy-space tuning, vertical E_{Field} are applied as examples. **a** WSe_2 homobilayer can change to direct gap under only the real-space tuning. **b** WS_2 homobilayer changes to direct gap under combined real and energy spaces tuning of $E_{\mathrm{Field}} = 0.2$ eV Å^{-1}. **c** The changes of E_{Diff} (ΔE_{Diff}) as a function of E_{Field}; for MoS_2/WS_2 the ΔE_{Diff} values are obtained from CB@K [refer to Supplementary Fig. 4c]. **d, e** Tuning trilayer to direct gap and the band edge real-space distributions as indicated by partial charge densities together with the percentage of the majority contributions.

which mix the band edges of different layers together (tends to equal distribution) and interlayer potential gradient which separate the charge densities of different layers (and the latter increase with distance), for VB@Γ 74% from the top layer while 25% comes from the middle layer. The contribution from the bottom layer to VB@Γ is missing, due to the potential energy difference between top and bottom layers is large (~0.8 eV, which is larger than the QB induced energy-splitting).

In addition to types (i) through (iv), we incorporated two additional groups: type-(v) WSSe/WSSe with different stacking (SSe-SeS, SSe-SSe or SeS-SeS, and SeS-SSe) and type-(vi) $W_{0.5}Mo_{0.5}Se_2/W_{0.5}Mo_{0.5}Se_2$. Real and/or energy spaces tuning were applied to them and the transition from indirect-to-direct gap are displayed in detail in Supplementary Note 7 (including Supplementary Figs. 9–11 and Supplementary Table 7).

More discussions

Efficient reducing of interlayer interactions, through increasing real-space interlayer separation and band edge energy-space difference, is of great advantageous for achieving a direct band gap in vdW stacked 2D semiconductors if the 2D monolayer has a direct gap. Importantly, both real and energy spaces tuning (large-angle twisting and dipole-layer vdW adsorption) can be permanently preserved without the need for external factors to maintain. In addition, if change the adsorbed dipole layer to a 2D ferroelectric layer[58], the direction of tuning can be inversed by electric field via the polarization reversal of ferroelectric layer, which gives the potential for reversible tuning between direct and indirect gaps. The reversible tuning between direct and indirect gaps is of great significance for 2D materials multiple applications. Note that the electric dipole from the adsorbed dipolar-layer can be either parallel or antiparallel to that from the heterolayers of TMDs, and the net electrical dipole is different for parallel and antiparallel conditions. Finally, the vdW adsorption of 2D metals with very high or low work functions, significant energy difference between layers can also be introduced by degenerate doping to the layer close to 2D metal[63].

Interestingly, one may estimate the critical E_{Field} for indirect–direct gap transition from some basic parameters but does not need the calculation with external electric field or with dipole-layer vdW adsorption. Namely, based on Fig. 2 above which relate ΔE with $E_{\text{Diff}}/|2t|$, and, the change rate of E_{Diff} with E_{Field} is known [Fig. 5c]. Note that t is already known, e.g., refer to Table 1. So, ΔE is now related to E_{Field}; and then the energy difference between ΔE_Γ and ΔVB, which is the ΔE to overcome for indirect–direct gap transition, can be related to E_{Field}. For example, for the WS_2 tetralayer with interlayer large-angle twisting, $\Delta E_\Gamma = |t| = 0.48$ eV for WS_2 tetralayer and ΔVB = 0.25 eV in WS_2 monolayer (Supplementary Fig. 12), and it can be estimated that the critical E_{Field} is <0.2 eV Å^{-1}; and DFT calculations with external electric field verified this (not shown). Details about the estimation method can be found in Supplementary Note 6.

The direct gap here for structures consisting of group VIB TMDs needs only the band edges tuning back to the K/K′ valley of the component layers, since robust ultrafast interlayer charge transfer has been generally observed in TMDs homo and heterostructures with random rotation angles[11,12,53]. There are two possible reasons for this: (1) the equivalence of K/K′ as shown in Supplementary Fig. 5. (2) Due to the small exciton radius of 2D materials[54], and hence excitons in 2D materials may only sensitive to the local structure and may not sensitive to the relative rotation between larger supercells.

Conclusions

In conclusion, we demonstrate that, to obtain direct gaps, the interlayer interaction can be reduced efficiently by real and energy spaces tuning. For the real and energy-space matched type-(i) homobilayers (larger $|t|$, $E_{\text{Diff}} = 0$), the interlayer interaction is the strongest and all have indirect band gaps without further tuning; while for the real energy-space mismatched type-(iii) heterobilayers (smaller $|t|$, $E_{\text{Diff}} \neq 0$), the interlayer interaction is the weakest and all show direct band gaps. Motived by this, the derived type-(iv) bilayers and few-layers are proposed with real and/or energy-space tuning to reduce the interlayer interaction and direct gaps are obtained in all systems. These tuning are efficient and hence bilayer and even few-layers can be tuned to direct gaps. The current work not only presents a systematic quantitative analysis of the interlayer interaction by tuning interlayer QB in both real and/or energy spaces but also offers efficient electronic properties tuning method via real and/or energy spaces for homo and heterostructures of TMDs and even other 2D semiconductors, and hence is of great significance for 2D materials' multiple applications.

Methods

First-principles simulations based on DFT[64] calculations were performed using the Vienna Ab initio Simulation Package (VASP)[65,66]. The projector augmented-wave potential[67,68] was adopted to describe the core electrons, and the valence electrons were described by plane-wave basis with an energy cut-off of 500 eV. The exchange-correlation functional adopted the generalized gradient approximation (GGA)[69] in the Perdew–Burke–Ernzerhof form (GGA-PBE). The SOC was included for electronic structure calculations, and the many-body dispersion[70–72] for vdW interaction was included for geometric structure optimization. The convergence criteria were 10^{-5} eV for the self-consistent energy calculation and 0.01 V/Å for the Hellmann–Feynman force in the geometric optimization. The BZ was sampled using Monkhorst–Pack scheme[73] with a k-point density of $2\pi \times 0.03$ Å^{-1}. The vacuum separation in the vertical direction was 15 Å to ensure that the interaction between periodic images is negligible. Dipole correction[74] is added for heterostructures. Our calculated direct or indirect band gaps are in excellent agreement with experiment, as evidenced in the case of $MoSe_2/WSe_2$[9,11]. Additionally, our analyses utilized several packages including Local Orbital Basis Suite Toward Electronic-structure Reconstruction (LOBSTER) package[75,76], VASPKIT[77], LEEDpat[78] and VESTA[79]. More details on LOBSTER can be found in Supplementary Note 4.

Data availability

The optimized structure mentioned in the paper can be downloaded from GitHub (https://github.com/T-M-Y-physics/Geometric-structures/tree/master). All other relevant data are available from the authors upon reasonable request.

Code availability

The software packages used for this study are standard and are outlined in the "Methods" section.

Received: 20 March 2024; Accepted: 5 September 2024;
Published online: 13 September 2024

References

1. Ramasubramaniam, A., Naveh, D. & Towe, E. Tunable band gaps in bilayer transition-metal dichalcogenides. *Phys. Rev. B* **84**, 205325 (2011).
2. Butler, S. Z. et al. Progress, challenges, and opportunities in two-dimensional materials beyond graphene. *ACS Nano* **7**, 2898–2926 (2013).
3. Geim, A. K. & Grigorieva, I. V. Van der waals heterostructures. *Nature* **499**, 419–425 (2013).
4. Padilha, J. E., Peelaers, H., Janotti, A. & Van de alle, C. G. Nature and evolution of the band-edge states in MoS_2: from monolayer to bulk. *Phys. Rev. B* **90**, 205420 (2014).
5. Liang, L. & Meunier, V. First-principles raman spectra of MoS_2, WS_2 and their heterostructures. *Nanoscale* **6**, 5394–5401 (2014).
6. Amin, B., Singh, N. & Schwingenschlögl, U. Heterostructures of transition metal dichalcogenides. *Phys. Rev. B* **92**, 075439 (2015).
7. Torun, E., Miranda, H. P. C., Molina-Sánchez, A. & Wirtz, L. Interlayer and intralayer excitons in MoS_2/WS_2 and $MoSe_2/WSe_2$ heterobilayers. *Phys. Rev. B* **97**, 245427 (2018).
8. Davies, F. H., Price, C. J., Taylor, N. T., Davies, S. G. & Hepplestone, S. P. Band alignment of transition metal dichalcogenide heterostructures. *Phys. Rev. B* **103**, 045417 (2021).

9. Ponomarev, E., Ubrig, N., Gutierrez-Lezama, I., Berger, H. & Morpurgo, A. F. Semiconducting van der waals interfaces as artificial semiconductors. *Nano Lett.* **18**, 5146–5152 (2018).
10. Kangsabanik, J., Svendsen, M. K., Taghizadeh, A., Crovetto, A. & Thygesen, K. S. Indirect band gap semiconductors for thin-film photovoltaics: high-throughput calculation of phonon-assisted absorption. *J. Am. Chem. Soc.* **144**, 19872–19883 (2022).
11. Hu, C., Naik, M. H., Chan, Y. H. & Louie, S. G. Excitonic interactions and mechanism for ultrafast interlayer photoexcited response in van der waals heterostructures. *Phys. Rev. Lett.* **131**, 236904 (2023).
12. Sun, C., Zhou, H., Sheng, T., Li, S. & Zhu, H. Ultrafast interlayer charge transfer outcompeting intralayer valley relaxation in few-layer 2D heterostructures. *ACS Nano* **18**, 931–938 (2023).
13. Ellis, J. K., Lucero, M. J. & Scuseria, G. E. The indirect to direct band gap transition in multilayered MoS_2 as predicted by screened hybrid density functional theory. *Appl. Phys. Lett.* **99**, 261908 (2011).
14. Komsa, H. P. et al. Two-dimensional transition metal dichalcogenides under electron irradiation: defect production and doping. *Phys. Rev. Lett.* **109**, 035503 (2012).
15. Terrones, H., Lopez-Urias, F. & Terrones, M. Novel hetero-layered materials with tunable direct band gaps by sandwiching different metal disulfides and diselenides. *Sci. Rep.* **3**, 1549 (2013).
16. Hong, X. et al. Ultrafast charge transfer in atomically thin MoS_2/WS_2 heterostructures. *Nat. Nanotechnol.* **9**, 682–686 (2014).
17. Komsa, H.-P. & Krasheninnikov, A. V. Native defects in bulk and monolayer MoS_2 from first principles. *Phys. Rev. B* **91**, 125304 (2015).
18. Bahadursha, N., Tiwari, A., Chakraborty, S. & Kanungo, S. Theoretical investigation of the structural and electronic properties of bilayer van der Waals heterostructure of Janus molybdenum di-chalcogenides – effects of interlayer chalcogen pairing. *Mater. Chem. Phys.* **297**, 127375 (2023).
19. Gong, Y. et al. Vertical and in-plane heterostructures from WS_2/MoS_2 monolayers. *Nat. Mater.* **13**, 1135–1142 (2014).
20. Chaves, A. et al. Bandgap engineering of two-dimensional semiconductor materials. *npj 2D Mater. Appl.* **4**, 29 (2020).
21. He, J., Hummer, K. & Franchini, C. Stacking effects on the electronic and optical properties of bilayer transition metal dichalcogenides MoS_2, $MoSe_2$, WS_2, and WSe_2. *Phys. Rev. B* **89**, 075409 (2014).
22. Chu, M., Sun, Y., Aghoram, U. & Thompson, S. E. Strain: a solution for higher carrier mobility in nanoscale MOSFETs. *Annu. Rev. Mater. Res.* **39**, 203–229 (2009).
23. Feng, J., Qian, X., Huang, C. W. & Li, J. Strain-engineered artificial atom as a broad-spectrum solar energy funnel. *Nat. Photonics* **6**, 866–872 (2012).
24. Han, Y. et al. Sub-nanometre channels embedded in two-dimensional materials. *Nat. Mater.* **17**, 129–133 (2018).
25. Khan, M., Tripathi, M. N. & Tripathi, A. Strain-induced structural, elastic, and electronic properties of 1L-MoS_2. *J. Mater. Res.* **37**, 3340–3351 (2022).
26. Scalise, E., Houssa, M., Pourtois, G., Afanas'ev, V. & Stesmans, A. Strain-induced semiconductor to metal transition in the two-dimensional honeycomb structure of MoS_2. *Nano Res.* **5**, 43–48 (2011).
27. Lu, N., Guo, H., Wang, L., Wu, X. & Zeng, X. C. Van der waals trilayers and superlattices: modification of electronic structures of MoS_2 by intercalation. *Nanoscale* **6**, 4566–4571 (2014).
28. Zhang, W., Wang, Q., Hu, L., Wu, J. & Shi, X. Electrical contacts to few-layer MoS_2 with phase-engineering and metal intercalation for tuning the contact performance. *J. Chem. Phys.* **154**, 184705 (2021).
29. Mirzakhani, M., Peeters, F. M. & Zarenia, M. Circular quantum dots in twisted bilayer graphene. *Phys. Rev. B* **101**, 075413 (2020).
30. Liao, M. et al. Precise control of the interlayer twist angle in large scale MoS_2 homostructures. *Nat. Commun.* **11**, 2153 (2020).
31. Liu, K. et al. Evolution of interlayer coupling in twisted molybdenum disulfide bilayers. *Nat. Commun.* **5**, 4966 (2014).
32. Bucko, J. & Herman, F. Large twisting angles in bilayer graphene moiré quantum dot structures. *Phys. Rev. B* **103**, 075116 (2021).
33. Latil, S., Amara, H. & Sponza, L. Structural classification of boron nitride twisted bilayers and ab initio investigation of their stacking-dependent electronic structure. *SciPost Phys.* **14**, 053 (2023).
34. Lu, N. et al. MoS_2/MX_2 heterobilayers: bandgap engineering via tensile strain or external electrical field. *Nanoscale* **6**, 2879–2886 (2014).
35. Kuc, A. & Heine, T. The electronic structure calculations of two-dimensional transition-metal dichalcogenides in the presence of external electric and magnetic fields. *Chem. Soc. Rev.* **44**, 2603–2614 (2015).
36. Guo, H., Lu, N., Dai, J., Wu, X. & Zeng, X. C. Phosphorene nanoribbons, phosphorus nanotubes, and van der waals multilayers. *J. Phys. Chem. C* **118**, 14051–14059 (2014).
37. Li, Y., Yang, S. & Li, J. Modulation of the electronic properties of ultrathin black phosphorus by strain and electrical field. *J. Phys. Chem. C* **118**, 23970–23976 (2014).
38. Splendiani, A. et al. Emerging photoluminescence in monolayer MoS_2. *Nano Lett.* **10**, 1271–1275 (2010).
39. Mak, K. F., Lee, C., Hone, J., Shan, J. & Heinz, T. F. Atomically thin MoS_2: a new direct-gap semiconductor. *Phys. Rev. Lett.* **105**, 136805 (2010).
40. Wang, Q. H., Kalantar-Zadeh, K., Kis, A., Coleman, J. N. & Strano, M. S. Electronics and optoelectronics of two-dimensional transition metal dichalcogenides. *Nat. Nanotechnol.* **7**, 699–712 (2012).
41. Kumar, A. & Ahluwalia, P. K. Electronic structure of transition metal dichalcogenides monolayers 1H-MX_2 (M = Mo, W; X = S, Se, Te) from ab-initio theory: new direct band gap semiconductors. *Eur. Phys. J. B* **85**, 186 (2012).
42. Lee, C. et al. Anomalous lattice vibrations of single- and few-layer MoS_2. *ACS Nano* **4**, 2695–2700 (2010).
43. Zhao, Y. et al. Extraordinarily strong interlayer interaction in 2D layered PtS_2. *Adv. Mater.* **28**, 2399–2407 (2016).
44. Kasai, H. et al. X-ray electron density investigation of chemical bonding in van der Waals materials. *Nat. Mater.* **17**, 249–252 (2018).
45. Le, N. B., Huan, T. D. & Woods, L. M. Interlayer interactions in van der waals heterostructures: electron and phonon properties. *ACS Appl. Mater. Interfaces* **8**, 6286–6292 (2016).
46. Chen, Y. T. et al. Interlayer quasi-bonding interactions in 2D layered materials: a classification according to the occupancy of involved energy bands. *J. Phys. Chem. Lett.* **12**, 11998–12004 (2021).
47. Hu, Z.-X., Kong, X., Qiao, J., Normand, B. & Ji, W. Interlayer electronic hybridization leads to exceptional thickness-dependent vibrational properties in few-layer black phosphorus. *Nanoscale* **8**, 2740–2750 (2016).
48. Shao, B., Jiang, X., Berges, J., Meng, S. & Huang, B. Engineering interlayer hybridization in energy space via dipolar overlayers. *Chin. Phys. Lett.* **40**, 087303 (2023).
49. Hsu, W. T. et al. Quantitative determination of interlayer electronic coupling at various critical points in bilayer MoS_2. *Phys. Rev. B* **106**, 125302 (2022).
50. Koo, J., Gao, S., Lee, H. & Yang, L. Vertical dielectric screening of few-layer van der Waals semiconductors. *Nanoscale* **9**, 14540–14547 (2017).
51. Shen, T. et al. Electric field screening in gate-tunable van der waals 2D-metal/InSe junctions. *Adv. Funct. Mater.* **32**, 2207018 (2022).
52. Mele, E. J. Commensuration and interlayer coherence in twisted bilayer graphene. *Phys. Rev. B* **81**, 161405 (2010).
53. Li, Y. et al. Tuning commensurability in twisted van der Waals bilayers. *Nature* **625**, 494–499 (2024).
54. Chichibu, S., Azuhata, T., Sota, T. & Nakamura, S. Spontaneous emission of localized excitons in InGaN single and multiquantum well structures. *Appl. Phys. Lett.* **69**, 4188–4190 (1996).
55. Chiu, M. H. et al. Determination of band alignment in the single-layer MoS_2/WSe_2 heterojunction. *Nat. Commun.* **6**, 7666 (2015).

56. Shi, X. Q. et al. C-60 on the Pt(111) surface: structural tuning of electronic properties. *Phys. Rev. B* **84**, 235406 (2011).
57. Harrison, W. A. *Elementary Electronic Structure* (World Scientific, London, 1999).
58. Shao, Y., Wang, Q., Pan, H. & Shi, X. Van der waals contact to 2D semiconductors with a switchable electric dipole: achieving both n- and p-type ohmic contacts to metals with a wide range of work functions. *Adv. Electron. Mater.* **6**, 1900981 (2019).
59. Kang, J., Zhang, L. & Wei, S. H. A unified understanding of the thickness-dependent bandgap transition in hexagonal two-dimensional semiconductors. *J. Phys. Chem. Lett.* **7**, 597–602 (2016).
60. Ren, M.-X. et al. Spin-dependent multilevel interactions at a nonmagnetic/magnetic $MoSe_2/VSe_2$ van der Waals interface and multifunctional properties. *Phys. Rev. B* **109**, 045420 (2024).
61. Zhang, Y.-J. et al. Momentum matching and band-alignment type in van der Waals heterostructures: Interfacial effects and materials screening. *Phys. Rev. B* **107**, 235420 (2023).
62. Chen, M. & Weinert, M. Layer k-projection and unfolding electronic bands at interfaces. *Phys. Rev. B* **98**, 245421 (2018).
63. Wang, Q., Dou, K. & Shi, X. Band alignment in multilayered semiconductor homojunctions supported on metals. *J. Mater. Chem. C.* **8**, 959–967 (2020).
64. Jones, J. R.O. Density functional theory: its origins, rise to prominence, and future. *Rev. Mod. Phys.* **87**, 897–923 (2015).
65. Kresse, G. & Furthmüller, J. Efficient iterative schemes for ab initio total-energy calculations using a plane-wave basis set. *Phys. Rev. B Condens. Matter* **54**, 11169–11186 (1996).
66. Hafner, J. Ab-initio simulations of materials using VASP: density-functional theory and beyond. *J. Comput. Chem.* **29**, 2044–2078 (2008).
67. Blöchl, P. E. Projector augmented-wave method. *Phys. Rev. B* **50**, 17953–17979 (1994).
68. Kresse, G. & Joubert, D. From ultrasoft pseudopotentials to the projector augmented-wave method. *Phys. Rev. B* **59**, 1758–1775 (1999).
69. Perdew, J. P., Burke, K. & Ernzerhof, M. Generalized gradient approximation made simple. *Phys. Rev. Lett.* **77**, 3865–3868 (1996).
70. Tkatchenko, A., DiStasio, R. A. Jr., Car, R. & Scheffler, M. Accurate and efficient method for many-body van der Waals interactions. *Phys. Rev. Lett.* **108**, 236402 (2012).
71. DiStasio, R. A., Gobre, V. V. & Tkatchenko, A. Many-body van der waals interactions in molecules and condensed matter. *J. Phys. Condens. Matter* **26**, 213202 (2014).
72. Hermann, J. & Tkatchenko, A. Density functional model for van der waals interactions: unifying many-body atomic approaches with nonlocal functionals. *Phys. Rev. Lett.* **124**, 146401 (2020).
73. Chadi, D. J. Special points for brillouin-zone integrations. *Phys. Rev. B* **16**, 1746–1747 (1977).
74. Makov, G. & Payne, M. C. Periodic boundary conditions inab initiocalculations. *Phys. Rev. B* **51**, 4014–4022 (1995).
75. Maintz, S., Deringer, V. L., Tchougreeff, A. L. & Dronskowski, R. LOBSTER: a tool to extract chemical bonding from plane-wave based DFT. *J. Comput. Chem.* **37**, 1030–1035 (2016).
76. Nelson, R. et al. LOBSTER: Local orbital projections, atomic charges, and chemical-bonding analysis from projector-augmented-wave-based density-functional theory. *J. Comput. Chem.* **41**, 1931–1940 (2020).
77. Wang, V., Xu, N., Liu, J. C., Tang, G. & Geng, W. T. VASPKIT: A user-friendly interface facilitating high-throughput computing and analysis using VASP code. *Comput. Phys. Commun.* **267**, 108033 (2021).
78. Hermann, K. & Van Hove, M. A. http://www.fhi-berlin.mpg.de/KHsoftware/LEEDpat/index.html (2022).
79. Momma, K. & Izumi, F. VESTA 3 for three-dimensional visualization of crystal, volumetric and morphology data. *J. Appl. Crystallogr.* **44**, 1272–1276 (2011).

Acknowledgements

This work was supported by the National Natural Science Foundation of China (Grants Nos. 12274111 and 12104124), the Central Guidance on Local Science and Technology Development Fund Project of Hebei Province (No. 236Z0601G), the Natural Science Foundation of Hebei Province of China (Nos. A2023201029, B2024201089), the Excellent Youth Research Innovation Team of Hebei University (No. QNTD202412), the Advanced Talents Incubation Program of the Hebei University (Grants Nos. 521000981390, 521000981394, 521000981395, 521000981423, and 521100221055), the Scientific Research and Innovation Team of Hebei University (No. IT2023B03), and the high-performance computing center of Hebei University.

Author contributions

X.-Q.S. and J.-L.W. conceived the project and revised the manuscript. M.-Y.T. performed the calculations and data analysis, made all figures, and wrote the draft of the manuscript. Y.-M.G., Y.-J.Z., and X.-H.L. checked the manuscript and provided suggestions. M.-X.R., K.-X.H., C.-D.J., H.Z., R.-Q.L., P.-L.G., and R.-N.W. provided technique supports. All authors analyzed the data and revised the final version of manuscript.

Competing interests

The authors declare no competing interests.

Additional information

Supplementary information The online version contains supplementary material available at https://doi.org/10.1038/s43246-024-00631-z.

Correspondence and requests for materials should be addressed to Jiang-Long Wang or Xing-Qiang Shi.

Peer review information *Communications Materials* thanks Nadire Nayir and the other anonymous, reviewer(s) for their contribution to the peer review of this work. A peer review file is available. Primary Handling Editors: Zakaria Al Balushi and Aldo Isidori.